Since January 2020 Elsevier has created a COVID-19 resource centre with free information in English and Mandarin on the novel coronavirus COVID-19. The COVID-19 resource centre is hosted on Elsevier Connect, the company's public news and information website.

Antiviral Research 174 (2020) 104661

Contents lists available at ScienceDirect

Antiviral Research

journal homepage: www.elsevier.com/locate/antiviral

Decoupling deISGylating and deubiquitinating activities of the MERS virus papain-like protease

Jozlyn R. Clasman[a], Renata K. Everett[a], Karthik Srinivasan[a], Andrew D. Mesecar[a,b,c,*]

[a] Department of Biological Sciences, Purdue University, West Lafayette, IN, USA
[b] Department of Biochemistry, Purdue University, West Lafayette, IN, USA
[c] Center for Cancer Research, Purdue University, West Lafayette, IN, USA

ARTICLE INFO

Keywords:
Coronavirus
Papain-like protease
PLpro
deISGylase
ISG15
Crystal structure

ABSTRACT

Coronavirus papain-like proteases (PLPs or PLpro), such as the one encoded in the genome of the infectious Middle East Respiratory Syndrome (MERS) virus, have multiple enzymatic activities that promote viral infection. PLpro acts as a protease and processes the large coronavirus polyprotein for virus replication. PLpro also functions as both a deubiquitinating (DUB) and deISGylating (deISG) enzyme and removes ubiquitin (Ub) and interferon-stimulated gene 15 (ISG15) from cellular proteins. Both DUB and deISG activities are implicated in suppressing innate immune responses; however, the precise role of each activity in this process is still unclear due in part to the difficulties in separating each activity. In this study, we determine the first structure of MERS PLpro in complex with the full-length human ISG15 to a resolution of 2.3 Å. This structure and available structures of MERS PLpro-Ub complexes were used as molecular guides to design PLpro mutants that lack either or both DUB/deISG activities. We tested 13 different PLpro mutants for protease, DUB, and deISG activitites using fluorescence-based assays. Results show that we can selectively modulate DUB activity at amino acid positions 1649 and 1653 while mutation of Val1691 or His1652 of PLpro to a positive charged residue completely impairs both DUB/deISG activities. These mutant enzymes will provide new functional tools for delineating the importance of DUB versus deISG activity in virus-infected cells and may serve as potential candidates for attenuating the MERS virus *in vivo* for modified vaccine design efforts.

1. Introduction

Interferon-stimulated gene 15 (ISG15) is a 17-kDa antiviral ubiquitin-like (Ubl) protein rapidly induced by type I interferons (IFNs) in response to viral infection (Durfee et al., 2010; Narasimhan et al., 2005). ISG15 contains two Ubl-folds connected by a short interdomain linker or hinge region, and like other Ubl proteins is conjugated to target proteins through an isopeptide linkage. The conjugation of ISG15 to target proteins is known as ISGylation, which is one of the critical mechanisms necessary for its antiviral activity. ISGylation involves the consecutive catalytic function of three interferon-induced enzymes: the E1 activating enzyme Ube1L, the E2 conjugating enzyme UbCH8, followed by the E3 ligase human HERC5. Although the biochemical functions associated with ISGylation are still under investigation (Giannakopoulos et al., 2009; Lai et al., 2009), a number of reports have now shown that ISG15 conjugation targets a broad range of viruses in an attempt to inhibit viral replication, including influenza A and B virus, Sindbis virus, HIV-1, herpes simplex-1, and murine herpesvirus (Zhao et al., 2013). One model for ISGylation involves a co-translational process where HERC5 conjugates free ISG15 onto newly synthesized viral proteins at the ribosome in order to disrupt their viral function (Durfee et al., 2010).

To help control ISG15 and its antiviral effector system, ISGylation can be reversed through the process of enzymatic deISGylation (deISG). For example, the host cell deISGylase ubiquitin-specific protease 18 (USP18) catalyzes the removal of ISG15 from target proteins in the cell. Recently, it was found that in humans, ISG15 deficiency actually increases resistance to viral infection *in vivo*. This is in contrast to what has been observed in mice, where ISG15 deficient mice are more susceptible to viral infection (Speer et al., 2016). Reports suggest that in humans, free extracellular ISG15 may be required to stabilize USP18 levels for temporal regulation of IFN-α/β signaling, a mechanism that

Abbreviations: Ub, ubiquitin; ISG15, interferon stimulating gene 15; PLpro, papain-like protease; DUB, deubiquitinating; PA, propargylamine; CoV, coronavirus; Ubl, ubiquitin-like; USP, ubiquitin specific protease

* Corresponding author. Department of Biological Sciences, Purdue University, West Lafayette, IN, USA.
E-mail address: amesecar@purdue.edu (A.D. Mesecar).

https://doi.org/10.1016/j.antiviral.2019.104661
Received 2 August 2019; Received in revised form 12 November 2019; Accepted 18 November 2019
Available online 23 November 2019
0166-3542/

may not exist in mice (Hermann and Bogunovic, 2017; Speer et al., 2016; Zhang et al., 2015). Speer et al. suggest that ISGylation may sequester free ISG15 early in infection to activate IFN, and only late in infection does USP18 become stabilized by free ISG15 to dampen IFN response. The role of free ISG15 and ISGylation in viral pathogenesis remains complex especially since free ISG15 is a negative regulator of IFN-signaling in humans (Perng and Lenschow, 2018). Interestingly, viruses have been shown to modulate the system by upregulating the process of deISGylation and increasing pools of ISG15, which could impact IFN activation. The expression level of USP18 was found to be elevated in patients infected with chronic hepatitis C virus (HCV) suggesting the possibility that HCV can modulate host-derived machineries to promote viral infection (Chen et al., 2005).

Other single-stranded RNA viruses such as coronaviruses (CoV) and arteriviruses have evolved their own viral-encoded deISGylating mechanisms to counteract the host ISG15/USP18 regulation system. For example, it was discovered that coronavirus papain-like proteases (PLpro) encode deISGylating and deUbiquitinating (DUB) catalytic activities in addition to their normal catalytic function which is to cleave the viral polyprotein at three sites between nsp1-2, nsp2-3, and nsp3-4. The additional DUB and deISGylating activities of PLpros are thought to contribute to the suppression of the innate immune response by acting on IFN-β and NF-κB signaling pathways (Clementz et al., 2010; Mielech et al., 2014; Ratia et al., 2014; van Kasteren et al., 2013). However, the precise role for each of these activities in antagonizing the innate immune response remains unclear due in part to the difficultly in separating these activities and characterizing each function in cell culture and *in vivo*.

In this study, we focus on PLpro from MERS-CoV because this highly pathogenic *betacoronavirus* still persists in the human population in contrast to the shorter-lived SARS-CoV (Chan et al., 2015). Since the initial outbreak in 2012, cases of MERS-CoV continue to be reported across 27 counties with the largest number of cases centralized in Saudi Arabia, United Arab Emirates, and the Republic of Korea (WHO, 2018). Approximately 35% of the reported patients infected with MERS-CoV have succumbed to the fatal respiratory disease (Fehr et al., 2017). As there are no antivirals or vaccines currently available, there is a critical need to understand the structural and molecular basis of virus-host interactions to facilitate the design of treatments against MERS-CoV infection.

Since PLpro is multifunctional in nature, it is an attractive target for protein engineering studies. For example, selectively removing PLpro DUB/deISG activities while maintaining its polyprotein cleavage activity is one strategy that could potentially be used for modified vaccine design through the development of an attenuated coronavirus. Designing different PLpro mutants that are DUB, deISG, or both DUB/deISG deficient would also be advantageous for functional studies in virus-infected cells to delineate how each activity contributes to virus replication and pathogenesis.

Our group first showed that it is possible to selectively modulate the SARS-CoV PLpro DUB and/or deISG activities without affecting its ability to cleave the *trans* nsp2-3 site by using structure-guided engineering (Ratia et al., 2014). Subsequently, our approach was translated to MERS-CoV PLpro using the structure of MERS-CoV PLpro in complex with Ub as a molecular guide (Bailey-Elkin et al., 2014). This study introduced mutations into the PLpro domain that disrupted its DUB activity in biochemical assays and in cell culture but its protease activity remained near wild type levels. However, since the PLpro mutants engineered in that study were only tested for DUB activity, it is still unclear if the high levels of deISG activity of PLpro were also affected and if both DUB as well as deISG of PLpro contributed to the activation observed in the IFN antagonism assays (Bailey-Elkin et al., 2014).

Another gap in our current knowledge exists in understanding the specificity of MERS-CoV PLpro for the full-length ISG15 protein. The structure of PLpro with a full-length ISG15 protein has yet to be determined. An X-ray structure of MERS-CoV PLpro bound to the C-terminal domain of human ISG15 (C-ISG15) has been reported but it lacks the N-terminal domain which is known to be important in binding SARS PLpro (Daczkowski et al., 2017b). The X-ray structure of mouse USP18 in complex with full-length mouse ISG15 has been determined, but USP18 has low sequence identity to PLpros. In addition, USP18 strictly recognizes ISG15 and has no recognition of Ub (Basters et al., 2017).

Here, we determined the X-ray structure of the first viral USP bound to the full-length human ISG15 protein to better differentiate the structural basis of MERS-CoV PLpro activity towards ISG15 versus Ub. We provide a detailed comparison between the ISG15 and Ub-bound complex as well as mutagenesis studies of key residues that may shed light on potentially eliminating both DUB/deISG activities of PLpro as well as selectively alternating PLpro substrate preference.

2. Materials and methods

2.1. Expression and purification of MERS-CoV PLpro-ΔUbl2

The MERS-CoV PLpro catalytic domain of nsp3 (residues 1544–1801 of the MERS viral polyprotein 1 ab) which is missing the Ubl domain was expressed from plasmid pEVL8-his8-TEVp-MERS-CoV PLpro-ΔUbl2 in *E. coli* BL21(DE3) by a modified version of Studier's autoinduction media using Super Broth supplemented with 0.2% lactose, 0.6% glycerol, and 0.05% glucose plus 50 μg/mL kanamycin described by Báez-Santos et al. (Báez-Santos et al., 2014; Studier, 2005). Cells were grown in 1 L cultures for 24 h at 25 °C after inoculation with a 10 mL starter culture as previously described (Clasman et al., 2017). Cells from four 1 L cultures were pelleted by centrifugation (6,440 × *g*, 4 °C, 30 min), and the resulting pellets from two 1 L cultures were distributed into two different 50 mL falcon tubes. Each pellet weighed approximately 16 g and 10 g, respectively. The pellets were stored at −80 °C until purification. Each pellet was removed from the −80 °C and purified separately by first thawing on ice and then resuspending in 5 mL of lysis buffer per 1 g of cells (Clasman et al., 2017). After resuspension, the cells were sonicated on ice with the same protocol as before but were lysed for a shorter 10 min duration (Clasman et al., 2017).

The lysed cells were clarified by centrifugation (26,200 × *g*, 4 °C, 45 min), and the supernatant was passed over a 5 mL HisTrap FF column (GE Healthcare) that was pre-charged with Ni^{2+} and equilibrated with 5 column volumes (CV) of 3% buffer B at 3 mL/min (Clasman et al., 2017). Weakly bound proteins were eluted from the column using 12 CV of 3% buffer B. Bound proteins, including his8-TEVp-MERS-CoV PLpro-ΔUbl2, were eluted from the column over a period of 33 min using a linear gradient of 20 CV starting at 3% buffer B and progressing to 100% buffer B while collecting 5 mL fractions. The fractions that showed absorbance at 280 nm on the chromatograms were analyzed by SDS-PAGE and for PLpro enzymatic activity. Those fractions judged to be most pure were combined and the final pools had volumes of 30 mL and 20 mL, respectively.

The N-terminal octa-his-tag was removed by dialyzing overnight each pool against 2 L of buffer A supplemented with tobacco etch virus protease (TEVp) at a ratio of 1 mg TEVp: 6 mg PLpro ratio. An overnight reaction is sufficient for removing the affinity tag by TEVp. The reaction was kept at 4 °C for a total of 96 h as ISG15-PA was prepared simultaneously. During dialysis, precipitation was observed, which predominantly contained contaminating proteins as assessed by SDS-PAGE. The dialyzed pools from each purification were passed separately and in tandem over a 5 mL HisTrap FF pre-charged Ni^{2+} column. The eluates containing the now untagged PLpro-ΔUbl2 in the flow-through were collected and the column was then washed using 5 CV of Buffer A. The flow-through and wash samples were combined and concentrated to ~2 mL at 6.3 mg/mL using an Amicon Ultra-15 Centrifugal Filter Unit (10 kDa MW cutoff). Concentrated MERS PLpro-

ΔUbl2 was then buffer exchanged into reaction buffer containing 10 mM Tris, pH 7.5, 5% glycerol, 10 mM BME using a PD-10 desalting column (GE Healthcare). The untagged and fresh (i.e. unfrozen and unstored) PLpro-ΔUbl2 was used immediately after purification for generating a fresh PLpro-ISG15 complex.

2.2. Expression and purification of human ISG15-PA

ISG15 propargylamine (ISG15-PA) was synthesized using the chitin intein-fusion method previously described by Wilkinson et al. (2005). Plasmid pTYB2-ISG15$_{1-156}$Cys78Ser was expressed in *E. Coli* BL21(DE3) cells by autoinduction for 24 h at 25 °C. A one liter Super Broth culture was inoculated with 10 mL of transformed *E. Coli* BL21(DE3) cells. After centrifuging (3011 × *g*, 20 min, 4 °C) the culture and discarding the supernatant, the harvested cells (~7 g) were frozen at −80 °C. On the day of purification, the cells were thawed and then resuspended in 50 mL chitin-column buffer (50 mM MES pH 6.5, 350 mM sodium acetate), supplemented with 50 μM PMSF. The resuspended cells were lysed on ice by sonication using a Branson Digital Sonifer (65% amplitude; 15 min, 5.5 s pulses, 5.5 s delays). The lysed cell debris was removed by centrifugation (28,960 × *g*, 30 min, 4 °C) and the supernatant (clarified lysate) was saved.

Chitin resin (20 mL in 20% ethanol, New England Biolabs) was transferred to a 150 mL fritted funnel and, using vacuum filtration, was equilibrated with 200 mL cold chitin-column buffer. The equilibrated chitin resin was transferred to a 100 mL beaker, combined with the clarified lysate (50 mL), and allowed to incubate with gentle stirring for 30 min at 4 °C. The chitin resin was then transferred back to the fritted funnel, and unbound proteins were washed using vacuum filtration with ten volumes of 50 mL column buffer. The resin was resuspended in 50 mL cold reaction buffer (50 mM MES pH 6.0, 350 mM sodium acetate, 122 mM sodium 2-mercaptoethanesulfonate (MESNa)), transferred to a beaker, and allowed to incubate at 4 °C overnight with gentle stirring.

The next day, the ISG15-MESNa that formed after the reaction was separated from the resin using vacuum filtration. The resin was then resuspended and washed with two 50 mL portions of column buffer to recover any residual ISG15-MESNa. The elution and washes were combined and concentrated to approximately 20 mL using an Amicon Ultra-15 Centrifugal Filter Unit (10 kDa MW cutoff). Approximately 0.3 g propargylamine HCl (Sigma-Aldrich) was added to the concentrated ISG15-MESNa at a 250 mM final concentration and 2.5 mL of 2 M NaOH was added dropwise to adjust the solution to pH 10. To generate ISG15-PA, the reaction was allowed to precede overnight at room temperature and the final reaction products were centrifuged (28,960 × *g*, 10 min, 4 °C) to remove any precipitation. The resulting supernatant was concentrated to approximately 2 mL and was buffer exchanged into reaction buffer using a PD-10 desalting column (GE Healthcare). Freshly generated ISG15-PA was used immediately for generating fresh PLpro-ISG15 complex. Ub-PA was also generated with a similar procedure as described above for probe reactivity assays. The only difference was that Ub-intein-CBD was expressed using *E. Coli* BL21(DE3) + RIPL cells, and protein was concentrated using 3 kDa MW cut-off Amicon device.

2.3. Generation and purification of MERS-CoV PLpro-ΔUbl2 in complex with human ISG15-PA

An incubation reaction containing 12.7 mg of PLpro-ΔUbl2 and 75 mg of human ISG15-PA (1 mg PLpro to 6 mg ISG15-PA) was allowed to react overnight at 4 °C in reaction buffer. These amounts of proteins were selected based on initial small-scale test reactions. Several attempts were used to separate the complex from free PLpro by passing the reaction over a 8 mL MonoQ 10/100 GL column (GE Healthcare), but regrettably free PLpro was not separated from the PLpro-ISG15 complex. The sample was assayed for Ub-AMC activity and 28% of the sample was determined to be free PLpro (~2 mg). To achieve 100% reacted PLpro-ISG15 complex, an additional 21 mg of ISG15-PA was added to the reaction mixture (1 mg PLpro to 10 mg ISG15-PA). The reaction mixture was kept at 4 °C for 72 h in MonoQ buffer A (10 mM Tris, pH 9.0, 5% glycerol, 10 mM BME) to ensure the complex was negatively charged for the final purification step. The reaction was passed over a final MonoQ column equilibrated with MonoQ buffer A, and unbound protein was washed with 3 CV of MonoQ buffer A. The PLpro-ISG15 complex was eluted with a linear gradient from 0 to 20% MonoQ buffer B (10 mM Tris, pH 9.0, 500 mM NaCl, 5% glycerol, 10 mM BME) for the duration of 64 min (20 CV), collecting 3 mL fractions at a flow rate of 2.5 mL/min. The final pool, shown in the additional file 1: Fig. S1A, was buffer exchanged into storage buffer (10 mM Tris, pH 7.5, 100 mM NaCl, 5% glycerol, 10 mM DTT) using a PD-10 desalting column and concentrated to 15.3 mg/mL using an Amicon Ultra-15 Centrifugal Filter Unit (30 kDa MW cutoff).

2.4. Crystallization and structure determination of PLpro-ISG15 complex

Freshly prepared PLpro-ISG15 complex was used to screen for initial crystallization conditions. A series of sparse-matrix crystallization screening solutions from Anatrace (Midwest Center for Structural Genomics (MCSG) screens-1-4) were used and sitting drops were formed using a Mosquito®Crystal liquid handling robot (TTP Labtech). Three protein concentrations (5 mg/mL, 10 mg/mL, 15.3 mg/mL) were dispensed in each of the three sub-wells in the 96–3 well sitting drop vapor diffusion plates (Greiner CrystalQuick crystallization plate) by adding 100 nL of purified PLpro-ΔUbl2-ISG15 complex to 100 nL of reservoir solution. The 200 nL protein drops were allowed to equilibrate against 50 μL reservoir solution at 20 °C in a Rigaku Minstrel® HT plate hotel and photos of each drop were recorded daily. An initial crystal hit from the MCSG-3 screen, containing 0.2 M potassium citrate tribasic, pH 8.3, 20% (w/v) PEG3350, was observed after 2 days. Initial crystals grew as thin plates with a hexagonal morphology (150 μm). This condition was optimized further using a 24-well sitting drop format with drops containing 1 μL of purified PLpro-ISG15 complex at 15.3 mg/mL and 1 μL reservoir. Optimization reagent, 2 M potassium citrate tribasic pH 8.3, was purchased from Anatrace, Inc. while a 50% PEG3350 solution was made from powder. Large crystals (> 500 μm) formed within 2 days in only a small subset of conditions, but many appeared as stacks of plates and macroscopically twinned. Large isolated crystals did form in a higher citrate concentration (0.35 M potassium citrate tribasic, pH 8.3, 22% (w/v) PEG3350), which were harvested.

To obtain more crystals for data collection, crystals were further optimized by macroseeding crystals into the clear drops in the same tray. Small microcrystals rapidly formed in the macroseeded drops and were subsequently used for transferring into another clear drop. Briefly, the microcrystals were looped with a 0.05–0.1 mm loop and quickly submerged into different clear drops. After transferring these microcrystals, single isolated hexagonal crystals (50 μm) formed within a few min and continued to grow to ~100–300 μm in size after 24–48 h at 20 °C. High quality crystals were grown using this technique. Crystals were grown in the same initial condition containing 0.2 M potassium citrate tribasic, pH 8.3, 20% (w/v) PEG3350 (additional file 1: Fig. S1B) and at a slightly higher citrate concentration (0.25 M potassium citrate tribasic, pH 8.3, 20% (w/v) PEG3350). Crystals were harvested using nylon loops, briefly soaked in cryoprotectant solution containing 20% glycerol, before flash-cooled into a vial submerged in liquid nitrogen. Vials were harbored in SPINE pucks during cryo-freezing and transported to the Advanced Photon source (APS) at Argonne National Laboratory (ANL).

X-ray data were collected on crystals of the PLpro-ISG15 complex at 100 K using a Dectris Eiger 9M detector (a 2°/s spindle rate) on beamline 21-ID-D at the Life Sciences-Collaborative Access Team (LS-CAT). Data were collected on three different crystals from the three

different conditions described above and each was indexed, processed, and scaled separately using HKL-3000 (Minor et al., 2006). To determine the initial phases for the PLpro-ISG15 complex, the PLpro domain from the bound PLpro-Ub complex (PDB accession code: **4RF1**) was used as a search model and the programs Phaser (McCoy et al., 2007) and Phenix were used to identify a molecular replacement solution. Free human ISG15 (Narasimhan et al., 2005) with the PDB accession code of **1Z2M** was manually positioned into the corresponding residual electron density using the program Coot (Emsley and Cowtan, 2004). The model was next refined using ridgid body refinement and the program Phenix.Refine (Afonine et al., 2012). Additional rounds of manual model building followed by coordinate and B-factor refinement were performed using the programs Coot and Phenix.Refine. Solvent molecules were added towards the end of model building and refinement which was ultimately complete when the R_{free} (21.5%) and R_{work} (17.2%) values plateaued at their minimums.

The atomic coordinates and structure factors for the MERS PLpro-ISG15 complex that crystalized at the lowest citrate concentration are deposited in the PDB with the accession code of **6BI8**. Figures were generated with Pymol (The Pymol Molecular Graphics System, 1.8.0 Schrödinger, LLC).

2.5. Expression and purification of MERS-CoV PLpro mutants

A series of 13 site-directed mutants were generated using the QuickChange™ site-directed mutagenesis system (Zheng et al., 2004) from Stratagene (La Jolla, CA). The wild-type pEVL8-his8-TEVp-MERS-CoV PLpro-ΔUbl2 plasmid was used as a template and primers were designed and synthesized using Integrated DNA Technologies (IDT). Correct mutations in the PLpro gene were confirmed by Sanger-based sequencing at the Purdue Genomics Core Sequencing Facility. Expression and purification of MERS-CoV PLpro mutant enzymes were performed by a modified procedure described above for the wild-type enzyme. For each of the mutant enzymes R1649A, H1652A, H1652F, V1691R, the pellets (12–15 g) from two 1 L cultures were harvested, and a two-day purification procedure was done using a Ni^{2+}-charged, 5 mL HisTrap FF column. Dialysis of the pooled fractions obtained from the Ni Hi-trap column was performed against 1 L of buffer A for 16 h at 4 °C using a 1:10 ratio of TEVp to PLpro in order to remove the N-terminal his-tag. The next day, the dialyzed sample was passed over the 5 mL Ni^{2+}-charged HisTrap FF column, and similar to the procedure above for purification of wild-type MERS PLpro, the flow-through as well as the wash were combined and concentrated. Instead of using a desalting column, the final pool was buffer exchanged into storage buffer using an Amicon Ultra-15 Centrifugal Filter Unit (10 kDa MW cutoff) and then concentrated to ~6–14 mg/mL. The final purified mutants were flash-frozen with liquid nitrogen at 100 K and stored in the −80 °C until their kinetic characterization.

The remaining mutants were expressed by autoinduction in 500 mL cultures using Super Broth media. Upon harvesting, the resulting pellets weighed ~3–5 g. Mutants were purified in parallel 2–4 mutants at a time. The pellets were resuspended in 50 mL lysis buffer, and the cells were lysed at a lower intensity and duration (5 min protocol at 65% amplitude with 6.6 s pulses and 9.9 s delays) before clarified by centrifugation (26,200 × *g*, 4 °C, 25 min).

The clarified lysates were passed over a Bio-Rad Econo-Pac® gravity column packed with a 3 mL HisPur™ Ni-NTA resin (Thermo Fisher Scientific), which was equilibrated with buffer A. Unbound proteins were washed from the column with a batch wash using 25 mL of buffer A and then with 25 mL of a lower percentage wash ranging from 12 to 30% Buffer B. Finally, the mutant PLpro was eluted with 25 mL of 50% of buffer B. All washes and elutions were tested for absorbance at 280 nm with a BioTek Take3™ Multi-Volume Plate and were pooled based on the presence of his-PLpro band at 31 kDa on the SDS-PAGE gel. As done with the other PLpro mutants, TEVp was added to the pooled samples before the pool was transferred to dialysis tubing (10 kDa MW cutoff), and dialyzed against 1 L buffer A for 16 h at 4 °C. To separate TEVp from the untagged PLpro mutant, the dialyzed sample was again passed over the gravity column equilibrated with buffer A. The flow-through containing untagged PLpro was collected as well as a 15–20 mL wash of buffer A. These samples were combined, and buffer exchanged into storage buffer using the Amicon Ultra-15 Centrifugal Filter Unit (10 kDa MW cutoff) before protein was concentrated to between 1 and 9 mg/mL. As done with the other PLpro mutants, samples were flash-frozen with liquid nitrogen and stored at −80 °C. It is important to note that the wild-type enzyme was also purified with this procedure and comparable specific activities values were obtained between protocols. An SDS-PAGE analysis of the wild-type and mutant MERS PLpro enzymes that were used for kinetics experiments is provided in additional file 1: Fig. S3.

2.6. Steady-state kinetic characterization of MERS PLpro wild-type and mutant enzymes

An initial screen to assess the catalytic activity of all 13 purified mutant PLpros and wild-type enzyme was performed at a single substrate concentration on three commercially available fluorogenic substrates; 50 μM Z-RLRGG-AMC (Bachem), 1 μM Ub-AMC (Boston Biochem/R&D Systems) and 1 μM ISG15-AMC (LifeSensors, Inc.). Each of these substrates contains the 7-amino-4-methylcoumarin (AMC) fluorescence group at the C-terminus. Fluorescence due to the release of the AMC group from the substrates was measured as described previously using a BioTEK Synergy H1 multimode microplate reader at 25 °C (Báez-Santos et al., 2014; Clasman et al., 2017). The reaction conditions i.e. plate-type and volume for each assay has been previously described in (Báez-Santos et al., 2014). Peptide hydrolysis was initiated with 0.75 μM of PLpro (final concentration) in reaction buffer (50 mM HEPES, 0.1 mg/mL BSA, 5 mM DTT). For the Ub-AMC and ISG15-AMC assays, reactions were initiated with 2.5 nM PLpro (final concentration) with the exception of H1652R, V1691R, and V1691K, which were initiated with a higher enzyme concentration of 0.83 μM (final concentration) due to lower turnover rates in cleaving both substrates which was initially observed during purification. The k_{cat}, i.e. turnover number, for each mutant and the wild-type enzyme were measured in triplicate for each fluorogenic substrate and at each substrate concentration. Rates were normalized to the wild-type as a relative percentage (%).

To more fully characterize each mutant with observable differences in catalytic rates, the steady-state kinetic parameters of the MERS-CoV PLpro wild-type and six mutants were determined for ISG15-AMC and Ub-AMC. Substrate concentration was varied from 0.19 μM to 6 μM for ISG15-AMC and from 0.38 μM to 12 μM for Ub-AMC. The reactions were initiated with 1.7 nM PLpro in both assays. For mutant enzymes showing observable saturation at higher substrate concentrations, the initial reaction rates were measured in duplicate and the averaged rates were plotted as a function of substrate concentration. These data were then fit to the Michaelis-Menten equation using non-linear regression and the enzyme kinetics module in SigmaPlot (version 12; Systat Software, Inc.). The kinetic parameters (k_{cat} and K_m) resulting from the fit of the data as well as the calculated value of k_{cat}/K_m for each enzyme were tabulated. The Val1691Ser enzyme could not be saturated with either the Ub-AMC or the ISG15-AMC substrates up to the highest concentrations tested. Saturation was also not observed with the Thr1653Arg enzyme using Ub-AMC as the substrate. In these cases, the initial reaction rates were plotted as a function of substrate concentration and the data were fit to a line using linear regression and the program GraphPAD Prism6 for the determination of the apparent k_{cat}/K_m.

2.7. Ub-PA and ISG15-PA probe reactivity assays with wild-type and mutant MERS PLpro

Probe reactivity assays were set-up at a 10 μL scale with pure MERS PLpro enzymes and PA probes. The reactivity of MERS PLpro wild-type was assessed with both PA probes at varying molar ratios. Ub-PA and human ISG15-PA were diluted in storage buffer containing fresh 10 mM DTT at final concentrations ranging from 5 to 25 μM and 25–100 μM, respectively. Each reaction was initiated with 5 μM MERS PLpro wild-type and allowed to react for 1 h at room temperature before quenching with 5X loading buffer (250 mM Tris-HCl pH 6.8, 50% glycerol, 10% SDS, 0.02% bromophenyl blue, and fresh 400 mM DTT). The reactivity of MERS PLpro wild-type and mutants were evaluated at single molar ratios of 5 μM PLpro and either 25 μM Ub-PA (1:5 M ratio) and 100 μM ISG15-PA (1:20 M ratio), which were quenched at different time points (2, 5, 30 min) with loading buffer. The entire reaction was loaded onto 4–20% Mini-PROTEAN® TGX™ precast SDS-PAGE gels from BioRad, and proteins were visualized with Coomassie Brilliant Blue staining.

3. Results and discussion

3.1. X-ray structure determination of the MERS PLpro-ISG15 complex

We determined previously that the core MERS-CoV PLpro-ΔUbl2 enzyme, i.e. without its adjacent N-terminal ubiquitin-like 2 (Ubl2) domain, is thermally stable, retains its full kinetic activity and substrate specificity profile and has an increased ability to readily form crystals that diffract to high resolution compared to the enzyme with the Ubl2 domain (Clasman et al., 2017). We therefore used the MERS-CoV PLpro-ΔUbl2 construct for the crystallization of the MERS-CoV PLpro-ISG15 complex, which was generated by reacting MERS-CoV PLpro-ΔUbl2 with the full-length, human ISG15 protein that was modified with a reactive, propargylamide (PA) group at its C-terminus. The PA group on ISG15 reacts with the catalytic cysteine and forms a covalent complex that can be readily purified (Supplementary Data: Fig. S1). From this point on, we will refer to the MERS-CoV PLpro-ΔUbl2 construct as simply “MERS-CoV PLpro” for simplicity.

Three complete X-ray datasets were collected on crystals of the MERS-CoV PLpro-ISG15 complex that were grown at three different citrate concentrations (0.2, 0.3 and 0.35 M). Unexpectedly, analysis of the electron density surrounding the Zn-finger motif for the PLpro-ISG15 complex crystals grown from 0.35 M citrate revealed no observable electron density for the Zn^{2+} atom in the Zn-finger motif even though these crystals diffracted to the same resolution and grew in the same space group as the crystals grown at the two lower citrate concentrations (Supplementary Data: Fig. S2). At citrate concentrations of 0.2 M and 0.25 M, the Zn^{2+} atom in the Zn-finger motif is clearly visible in electron density suggesting that the higher concentrations of citrate chelated the Zn^{2+} and thereby depleted it from the Zn-finger. Therefore, the X-ray structure of the MERS-CoV PLpro-ISG15 complex grown from crystals at 0.2 M citrate was determined to a resolution of 2.3 Å (R_{work} = 17.1% and R_{free} = 21.5%). A summary of the X-ray data collection and refinement statistics are provided in Table 1. The enzyme crystallized in space group R3 with two identical copies of the PLpro-ISG15 complex in the asymmetric unit. The PLpro chains from each dimer were virtually identical with a RMSD of 0.08 Å over Cα atoms from 255 residues while human ISG15 exhibited slightly more conformational diversity with a RMSD of 0.8 Å over 151 Cα positions.

3.2. Interactions of MERS-CoV PLpro with ISG15

The interactions between MERS-CoV PLpro and ISG15 are predominantly centralized to the ubiquitin recognition subsite S1 (SUb1) of PLpro (Ratia et al., 2014) which is composed of residues at the interface between the fingers and thumb domains (Fig. 1A). Both water-mediated and hydrophobic interactions are observed in the contacting regions (Fig. 1A). The water-mediated network is predominately formed by main-chain interactions between the carbonyl groups of Lys1686 and Cys1689 in the fingers domain of PLpro and the carboxyl side chain groups of Glu127 and Gly128 of ISG15 (Fig. 1B). The side-chain of Lys129 in ISG15 also participates in a water-mediated interaction with MERS-PLpro.

Van der Waals interactions between the Cβ atom of His1652 and residues Pro130 and Trp123 are also observed forming a small hydrophobic pocket (Fig. 1C). Trp123 of ISG15 is sandwiched between the aliphatic chain of Arg1649 of PLpro and the hydrophobic side-chain of Val1691, which also interacts with the alkyl group of Thr125 of ISG15. Apart from Thr125, which is unique to human ISG15, the proline and tryptophan residues are conserved among species of ISG15, and appear to be utilized for interactions by a wide range of deISGylases, both in the USP and ovarian tumor family (vOTU), suggesting that this region of PLpro may be critical for ISG15 recognition (Akutsu et al., 2011; Basters et al., 2017; Daczkowski et al., 2017a).

Surprisingly, there are no strong interactions between the N-terminal domain of ISG15 and the ridge helix of PLpro (Fig. 1A), which is the first helix of the thumb domain, adjacent to that of the Ubl2 domain in PLpros (Ratia et al., 2014). After data refinement, residue Lys1550 of the ridge helix of MERS-CoV PLpro and Gln34 of ISG15 appeared to be within hydrogen bonding distance (Fig. 2B). However, electron density

Table 1
Data collection and refinement statistics of MERS PLpro-ISG15 complex.

MERS-CoV PLpro-ISG15	
Data collection	
Beamline	21-ID-D
Wavelength (Å)	0.987
Space group	*R3*
Unit cell dimensions:	
a, b, c (Å)	*148.035, 148.035, 134.189*
α, β, γ (°)	*90, 90, 120*
Resolution (Å)	100–2.30 (2.34–2.30)[a]
Number of reflections observed	2377975
Number of unique reflections	49135
R_{merge} (%)[b]	10.0 (56.0)
R_{pim} (%)[c]	5.8 (33.7)
$CC_{1/2}$ *(%) in highest shell*	73.2
CC (%) in highest shell*	91.9
$I/\sigma I$	20.2 (2.79)
% Completeness	98.6 (99.0)
Redundancy	3.8 (3.6)
Refinement	
Resolution range (Å)	42.734–2.291 (2.348–2.291)
No. of reflections in working set	48445
No. of reflections in test set	2006
R_{work} (%)[d]	17.15 (20.84)
R_{free} (%)[e]	21.50 (27.12)
Wilson B factor (Å^2)	30.81
Average B factor (Å^2)	44.9
RMSD from ideal geometry	
Bond length (Å)	0.013
Bond angle (deg)	1.06
Ramachandran plot	
Most favored (%)	94.88
Allowed (%)	4.38
Disallowed (%)	0.73

[a] Values in parentheses are for the last (highest resolution) shell.

[b] $R_{merge} = \sum_{hkl}\sum_i |I_i(hkl) - \langle I(hkl)\rangle| / \sum_{hkl}\sum_i I_i(hkl)$, where $I_i(hkl)$ is the intensity of a given reflection, and $I(hkl)$ is the mean intensity of symmetry-related reflections.

[c] $R_{pim} = \sum_{hkl}\sqrt{\left(\frac{1}{n}-1\right)}\sum_i |I_i(hkl) - \langle I(hkl)\rangle| / \sum_{hkl}\sum_i (hkl)$, where n is the multiplicity for multiplicity-weighted R_{merge}.

[d] $R_{work} = \sum_{hkl} ||F_{obs}| - |F_{calc}|| / \sum_{hkl} |F_{obs}|$, where F_{obs} and F_{calc} are the observed and calculated structure factors, respectively.

[e] R_{free} was calculated using 4% of the data set chosen at random that were excluded from the refinement.

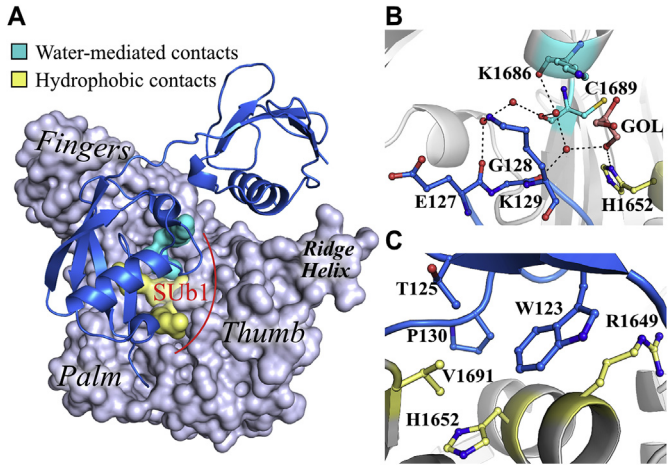

Fig. 1. PLpro SUb1 subsite and ISG15 interactions involve both water-mediated and hydrophobic contacts. (A) Structure of PLpro-ISG15 complex. PLpro is shown as a gray surface representation with water-mediated and hydrophobic surface residues colored in cyan and yellow, respectively. ISG15 is shown as a blue cartoon representation where only the C-terminal domain of ISG15 contacts PLpro SUb1 subsite. (B) Close-up view of water-mediated network (cyan) shows peptide backbone and side-chains of Lys129 of ISG15 (blue sticks) and His1652 of PLpro (yellow sticks) coordinating water molecules (red spheres) and a glycerol (GOL, pink sticks) molecule between PLpro and ISG15. (C) Magnified view of hydrophobic contacts (yellow) where no solvent molecules are present. Trp123, Pro130, and Thr125 of ISG15 (blue sticks) are accommodated to form a hydrophobic pocket with MERS-CoV PLpro. Atoms in Panels B–C are colored as follows; nitrogens (dark blue), oxygens (red), sulfur (yellow) carbons (light blue).

associated with these side-chains, especially Gln34 of ISG15 is weak suggesting that these residues may not interact (Fig. 2B). To test this hypothesis, Lys1550 was mutated to an alanine residue as well as the equivalent phenylalanine residue of the ubiquitin recognition subsite S2 (SUb2) in SARS PLpro and no differences were observed in the k_{cat} values for the response of MERS-CoV Lys1550Ala and Lys1550Phe to the substrate ISG15-AMC compared to wild type (Fig. 4A).

3.3. Structural differences in recognition of ISG15 and Ub by MERS-CoV PLpro

To identify potential residues of MERS-CoV PLpro that dictate substrate specificity for ISG15 versus Ub, the MERS-CoV PLpro-ISG15 structure was superimposed with the Ub-bound structure (PDB accession code **4RF1**) and the result is shown in Fig. 3. The C-terminal domain of ISG15 (residues 82–156) and Ub (residues 1–75) superimpose quite well with a RMSD of 0.95 Å over 75 Cα atoms and the PLpro structures superimpose with a RMSD of 1.16 Å over 252 Cα atoms (Fig. 3A). As expected, PLpro interacts with RLRGG residues at the C-terminus of both ISG15 and Ub substrates in a nearly identical manner by utilizing an intricate hydrogen-bonding network mainly composed of main-chain interactions (Fig. 3B–D). These interactions were described previously for Ub (Bailey-Elkin et al., 2014) with one minor difference in the orientation of Arg155 of ISG15 (equivalent to Arg74 of Ub) as shown in Fig. 3D. Arg155 of ISG15 corresponds to X in the P3 position of the LXGG substrate recognition sequence of PLpro. In the Ub-bound structure, the side-chain η-amino group of Arg74 is hydrogen-bonded to the main-chain carbonyl of Thr1755, which is found in the substrate-binding loop of MERS-CoV PLpro, while in ISG15, triethylene glycol (PGE) is bound in place of the Arg74 side-chain (Fig. 3B and C). Instead, Arg155 of ISG15 undergoes a ~122° flip and interacts with the main-chain carbonyl of Pro1644 in the adjacent loop of the thumb domain between PLpro helix α6-α7 (secondary structure numbering based on (Lei et al., 2014)). This alternative conformation of Arg155 was also observed in the structure of MERS-CoV PLpro in complex with only the C-terminal domain of ISG15 (Daczkowski et al., 2017b). Therefore, there is observable flexibility for Arg in the P3 position in adopting different contacts with PLpro.

In both ISG15-and Ub-bound structures, the guanidinium group of Arg1649 in PLpro forms a stacked interaction with the guanidinium group of Arg153 (equivalent to Arg72 of Ub), which is P5-Arg of the RLRGG motif (Fig. 3E, region #1). However, structural differences are observed with residues surrounding Arg1649. In the Ub-bound complex, Arg42 of Ub positions itself to alleviate charge-charge repulsion with Arg1649 while in ISG15, Trp123 forms a more favorable interaction with Arg1649 by packing against its aliphatic chain. Another difference observed between ISG15 and Ub-bound structures is that Thr1653 only forms direct hydrogen-bond interactions with Gln49 (equivalent to Pro130 of ISG15) and Glu51 (equivalent to Glu132 of ISG15) in the Ub-bound complex whereas in the ISG15-bound complex Thr1653 forms no direct interactions (Fig. 3E, region #1). Interestingly, in the structure of MERS-CoV with full-length ISG15, Glu132 of ISG15 does not appear to make strong contacts with PLpro. Though Glu132 was noted as a 'principle electrostatic interaction' in the structure of MERS-PLpro with N-terminally truncated ISG15, it forms a fairly weak electrostatic interaction (~3.8 Å) with Lys1657 in the full-length ISG15 structure, which was only adopted in a single monomer. Thus, the presence of the N-terminal domain in full-length ISG15 influences interactions of the C-terminal domain of ISG15 with PLpro.

Another common feature between the ISG15 and Ub bound MERS-CoV structures is that Val1691 of PLpro forms Van der Waals contacts with Ile44 in the Ub hydrophobic patch and Thr125 in ISG15 (Fig. 3E, region #2). In ISG15, however, this hydrophobic 'patch' appears to be

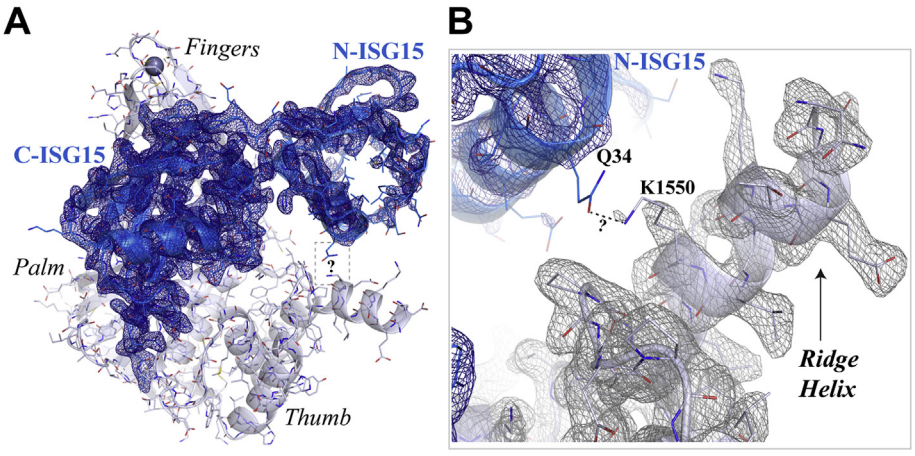

Fig. 2. Electron density maps reveal that the N-terminal domain of ISG15 (blue) has more flexibility and weakly associates with MERS-CoV PLpro (gray). (A) Overall structure of PLpro with the three subdomains labeled bound to ISG15. $2F_o$-F_c electron density map of the complete ISG15 (blue mesh) is contoured to 1σ, which show that N-terminal domain of ISG15 (N-ISG15) has a weaker overall density map compared to the C-terminal domain of ISG15 (C-ISG15). PLpro and ISG15 are shown as a cartoon with residues represented as lines. A gray dotted box highlights the region of interest. (C) Magnified view of 'Ridge Helix' (arrow), and its corresponding $2F_o$-F_c electron density map (gray mesh) contoured to 1σ, and N-ISG15 reveals one interaction in hydrogen bonding distance (dotted lines), which was observed after data refinement. Weak side-chain densities pose the question on if there is a direct interaction, which is illustrated with a question mark.

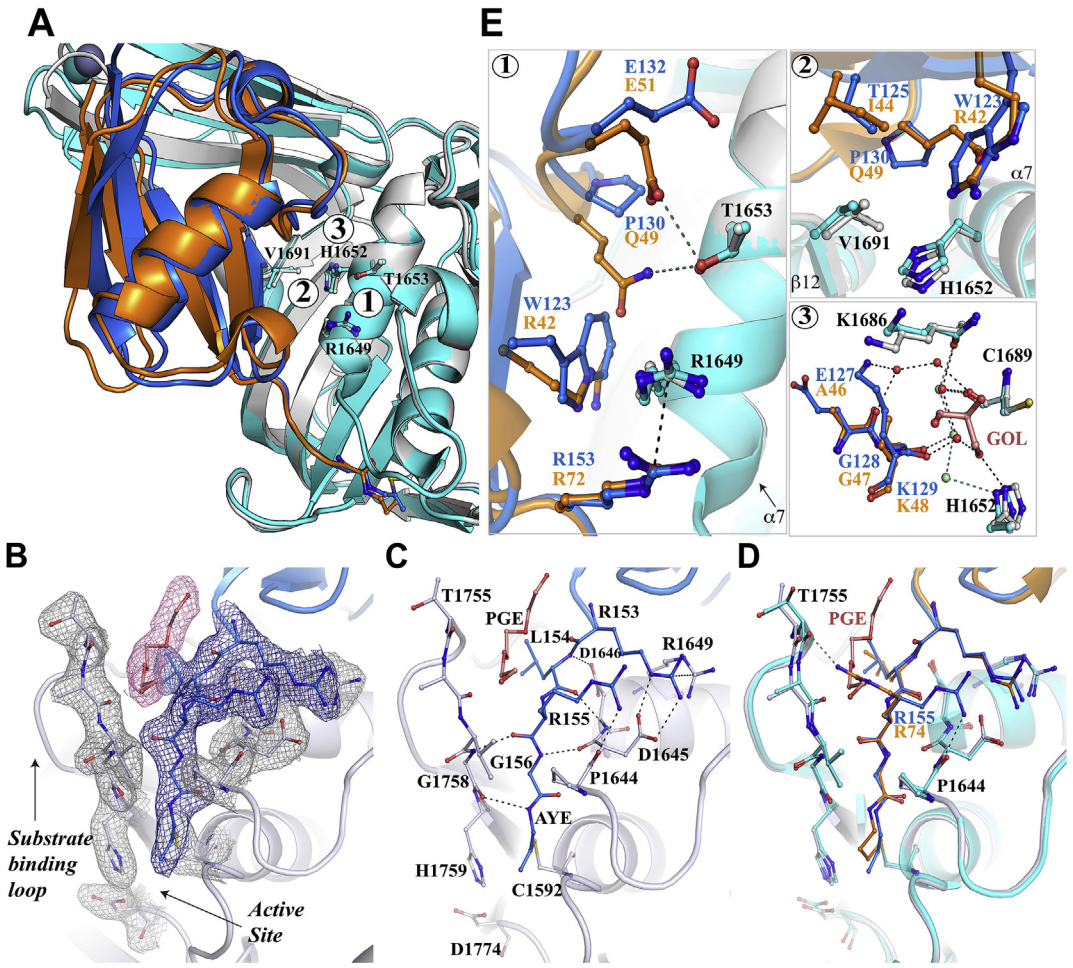

Fig. 3. Superposition of X-ray crystal structures of MERS-CoV PLpro (gray, PDB code **6BI8**) bound to ISG15 (blue) and MERS-CoV PLpro (cyan, PDB code **4RF1**) bound to Ub (orange). (A) Overall view of the shared Ub and C-ISG15 binding pocket with key PLpro SUb1 subsite interactions designated 1–3. Region 1; interactions involving Arg1649 and Thr1653 of PLpro. Region 2; hydrophobic interactions involving His1652 and Val1691 of PLpro. Region 3; water-mediated interactions starting at His1652 of PLpro. (B) $2F_o$-F_c electron density maps are contoured to 1 σ and reveal strong data for interacting residues of the substrate-binding loop, adjacent loop between helix α6-α7, and catalytic triad of PLpro as well as the RLRGG motif of ISG15. (C) Hydrogen bonding network interactions between PLpro and RLRGG motif of ISG15 (represented as black dashed lines). AYE; allyamine. PGE; triethylene glycol. (D) Overlay of MERS-CoV PLpro-ISG15 and –Ub active site interactions reveals a difference in conformation for the Arg155 side-chain of ISG15 (equivalent to Arg74 of Ub) due to a bound PGE molecule. Black and cyan dashes represent hydrogen bonds in the PLpro-ISG15 and –Ub complex, respectively. (E) Magnified views of key interactions (1–3) in both structures. Bonding residues of PLpro to ISG15 and Ub are shown as black or cyan dashed lines, respectively. Region 1; Interactions with PLpro α7 show that Arg1649 orientations are shared while Thr1653 only interacts with Ub. Arg1649 easily accommodates Trp123 of ISG15 while the charged Arg42 of Ub may not be favored. Region 2; Residues of PLpro α7 and β12 form a larger hydrophobic pocket with Trp123 and Pro130 of ISG15. Hydrophobic contacts between Val1691 are shared at equivalent position Thr125 of ISG15. Region 3; His1652 imidazole and peptide backbone residues of PLpro coordinate solvent molecules in a similar fashion to a conserved glycine residue. Less water (cyan spheres) molecules are observed in the Ub-bound structure while in the ISG15-bound structure more waters (red spheres) and a glycerol (GOL, pink sticks) molecule was observed.

extended by Trp123 and Pro130, thus allowing His1652 of PLpro to also engage in an interaction. As previously noted by Basters et al. for USP18, this region of ISG15 is conserved across different ISG15 species and was proposed to be a unique hydrophobic patch to ISG15 differing from the well-known hydrophobic patch of Ub, which is commonly utilized for recognition by a vast number of Ub-binding proteins (Basters et al., 2017; Komander and Rape, 2012). Our observations and those of others collectively support the hypothesis that this hydrophobic region of ISG15 may be a canonical recognition region that is utilized in general by deISGylases to specifically recognize ISG15.

Finally, the water-mediated contacts involving the side-chain imidazole of His1652 are also conserved between ISG15 and Ub bound MERS-CoV PLpro structures (Fig. 3E, region #3). Although the interactions appear more extensive in the PLpro-ISG15 complex, His1652 of MERS-CoV PLpro is observed to bridge with a water molecule back to the main-chain carboxyl of a glycine residue, Gly47 of Ub or Gly128 of ISG15, in both structures. A similar water-mediated network was also observed in the SARS-CoV PLpro-Ub aldehyde structure suggesting that this is a canonical region where intervening solvent molecules bridge indirect interactions between the substrate and the protease (Ratia et al., 2014).

3.4. Structure-guided design of MERS-CoV PLpro mutants

Structure-guided engineering of SARS-CoV PLpro has been shown to be a viable strategy for selectively decoupling SARS PLpro DUB and/or deISG activities while maintaining the ability of the enzyme to efficiently process the polyprotein (Bailey-Elkin et al., 2014; Ratia et al., 2014). We therefore sought to use our MERS-CoV PLpro bound ISG15 structure and the previously determined Ub-bound structures to design a set of MERS-CoV PLpro mutants that are either DUB or deISG deficient, or both DUB and deISG deficient. The ultimate goal is to design

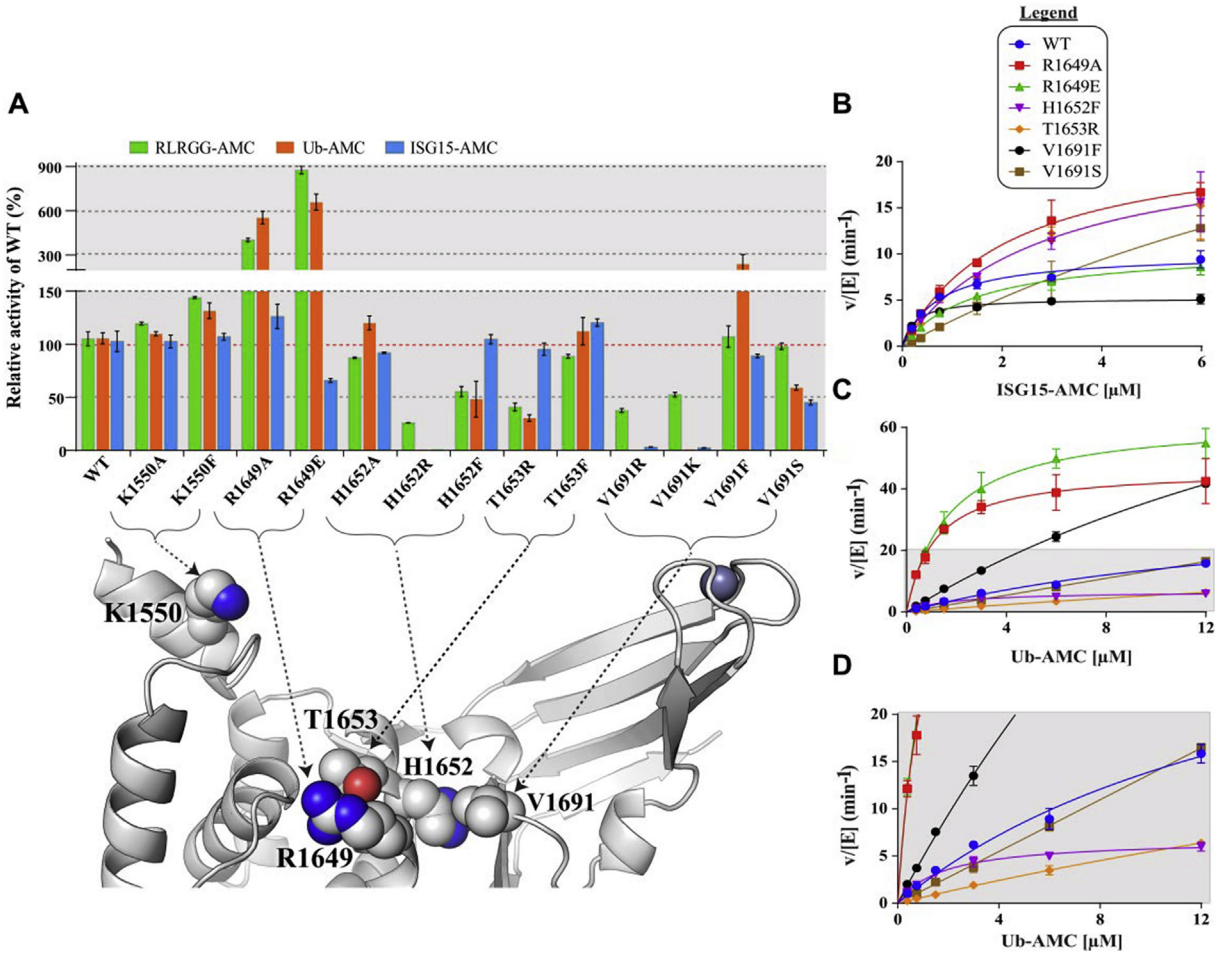

Fig. 4. Initial and complete kinetic characterization of MERS-CoV wild-type and mutants. (A) Initial assessment of catalysis against three ubiquitin-based fluorogenic substrates at a single substrate concentration: 50 μM RLRGG-AMC (green), 1 μM Ub-AMC (orange), and 1 μM ISG15-AMC (blue). PLpro mutants are plotted as a function of relative activity of the wild-type (%) based on the calculated turnover number. Error bars represent standard deviations calculated from triplicate measurements. The location of each residue side-chain position of PLpro (spheres) used for mutagenesis is shown in the structural representation of PLpro (gray). ISG15 was omitted for clarity. (B-D) Kinetic rate (velocity/[Enzyme]) of the wild-type and six mutants to increasing ISG15-AMC (B) and Ub-AMC (C-D) concentrations. Gray shaded box in panel C is magnified for clarity in panel D. All data were fit to the Michaelis-Menten equation with the exception of Thr1653Arg and Val1691Ser, where data failed to reach saturation and were fit to a linear regression equation. Error bars represent a range from duplicate measurements.

mutants that will serve as tools to delineate the function of DUB versus deISG activities in virus-infected cells and for potentially generating attenuated virus strains for the purpose of creating a live-attenuated MERS-CoV vaccine. We focused our mutagenesis on the following MERS-CoV PLpro residues; Arg1649, His1652, Thr1653, and Val1691, which all reside in the MERS-CoV PLpro SUb1 subsite. Mutants were designed based on two approaches: (i) alanine-scanning mutagenesis to completely remove interactions, and (ii) insertion of a bulky or charged residue to create steric hindrance, i.e. unfavorable Van der Waals overlap, or electrostatic repulsion to disrupt contacts. Additionally, we sought to engineer MERS-CoV PLpro to be more SARS-like, as Lys1550Phe and Arg1649Glu were mutated based on the equivalent residue found in SARS-CoV PLpro to decipher the residues that contribute to SARS-CoV PLpro enhanced turnover rate compared to MERS-CoV PLpro for different substrates (Báez-Santos et al., 2014).

First, we performed an initial assessment of the kinetic activity of 13 PLpro mutants at a single substrate concentration by testing their ability to hydrolyze three commercially available fluorogenic substrates commonly used to evaluate PLpro protease, DUB, and deISG activities. Results from the initial assessment are summarized in Fig. 4A as the percent relative activity to the wild-type enzyme. Mutants that did not exhibit a significant alteration in kinetic activity towards any of the three substrates include Lys1550Ala, Lys1550Phe, His1652Ala and Thr1653Phe. Mutants that did show reduced peptide hydrolysis and severely impaired hydrolysis for both DUB/deISG activities were His1652Arg, Val1691Arg, and Val1691Lys. Val1691Ser displayed ~50% reduction in both DUB/deISG activities, but the peptide hydrolysis of this mutant was similar to the wild-type. Surprisingly, Arg1649Ala and Arg1649Glu exhibited enhanced hydrolysis towards both the Ub-AMC and the peptide substrates while the activity towards ISG15-AMC was not significantly altered. Compared to these mutants, Val1691Phe exhibited moderately enhanced Ub-AMC activity. Finally, His1652Phe and Thr1653Arg showed ~30–50% Ub-AMC and the peptide activities but maintained ISG15-AMC activity.

To confirm observed trends and to more fully characterize the kinetic properties for the Arg1649Ala, Arg1649Glu, His1652Phe, Thr1653Arg, Val1691Phe, and Val1691Ser mutants, the kinetic parameters k_{cat} and K_m were determined for each of these mutants with the substrates Ub-AMC and ISG15-AMC and the results are summarized in Table 2 along with the parameters previously determined for other mutants (Daczkowski et al., 2017b). The catalytic efficiency (k_{cat}/K_m) and the selectivity ratio (k_{cat}/K_m for ISG15-AMC divided by k_{cat}/K_m for Ub-AMC, and vice versa) for each mutant was also calculated and is compared to the wild-type. From these data, it is observed that mutating the ridge helix residue Lys1550 to either an alanine or the equivalent phenylalanine residue in SARS-CoV PLpro, had no

Table 2
Summary of kinetic parameters of fully characterized PLpro mutants.

Mutant	K_m (μM)	k_{cat} (min^{-1})	Fold activity	k_{cat}/K_m (μM^{-1} min^{-1})	Fold efficiency	Selectivity
ISG15-AMC[a]						
WT	0.73 ± 0.10	10.05 ± 0.44	1.0	13.81 ± 2.04	1.0	6.2
R1649A	2.16 ± 0.33	22.84 ± 1.51	2.3	10.60 ± 1.76	0.8	0.3
R1649E	1.50 ± 0.21	10.69 ± 0.57	1.1	7.13 ± 1.06	0.5	0.2
H1652F	2.80 ± 0.69	22.65 ± 2.63	2.3	8.08 ± 2.20	0.6	2.1
T1653R	2.82 ± 0.74	22.73 ± 2.80	2.3	8.07 ± 2.33	0.6	12.5
K1657E[b]	N.S.[c]	N.S.	N.S.	0.74 ± 0.17	0.1	0.2
V1691F	0.25 ± 0.04	5.20 ± 0.17	0.52	20.80 ± 3.13	1.5	4.1
V1691D[b]	N.S.	N.S.	N.S.	0.23 ± 0.05	0.017	0.1
V1691S	N.S.	N.S.	N.S.	2.23 ± 0.10	0.2	1.6
Ub-AMC[a]						
WT	16.58 ± 4.20	37.07 ± 6.21	1.0	2.24 ± 0.68	1.0	0.2
R1649A	1.13 ± 0.20	46.51 ± 2.36	1.3	41.31 ± 7.58	18.5	3.9
R1649E	1.65 ± 0.21	62.62 ± 2.57	1.7	37.93 ± 5.08	17.0	5.3
H1652F	1.77 ± 0.21	6.76 ± 0.26	0.2	3.81 ± 0.47	1.7	0.5
T1653R	N.S.	N.S.	N.S.	0.55 ± 0.01	0.2	0.1
K1657E[b]	3.17 ± 0.37	12.22 ± 0.43	0.3	3.85 ± 0.12	1.7	5.2
V1691F	26.17 ± 3.01	132.30 ± 11.29	3.6	5.06 ± 0.72	2.3	0.2
V1691D[b]	10.04 ± 2.33	29.44 ± 2.40	0.8	2.93 ± 0.25	1.3	12.7
V1691S	N.S.	N.S.	N.S.	1.37 ± 0.02	0.6	0.6

[a] Steady-state values were determined from duplicate measurements, reported as a mean ± standard error.
[b] Kinetic parameters from Daczkowski, C.M. et al. 2017b.
[c] NS, enzyme not saturated. k_{app} values reported as a slope ± best-fit error from a linear regression were used to approximate k_{cat}/K_m.

significant effect on the functionality of MERS-CoV PLpro (Fig. 4A). This result supports our prediction that the potential hydrogen bond observed after data refinement between Lys1550 of PLpro and Gln34 of ISG15 is unlikely and not important for ISG15 recognition. This observation stands in stark contrast to SARS-CoV PLpro that has two ubiquitin recognition sites (SUb1 and SUb2) for ISG15 and K48-linked diUb chains (Békés et al., 2016; Ratia et al., 2014). Based on the PLpro-ISG15 recognition model proposed by Ratia et al., SARS-CoV PLpro may utilize its ridge helix to directly engage with the N-terminal domain of ISG15 (Ratia et al., 2014). Our results indicate that MERS-CoV PLpro does not possess an equivalent SUb2 subsite.

The data in Fig. 4A also suggest that the residue in position 1691 of the PLpro SUb1 subsite is very sensitive to charge, polarity, and the size of the amino acid introduced into this position. Adding a negatively charged aspartate residue at this position was shown to selectively disrupt the recognition of ISG15-AMC by MERS PLpro while the ability to recognize and hydrolyze Ub-AMC was maintained (Daczkowski et al., 2017b). The aspartate is likely able to make a salt bridge with Arg42 of Ub while in ISG15, the hydrophobic pocket cannot accommodate this charged residue. In contrast, substituting a positively charged arginine or lysine at this position severely impairs both activities of PLpro. For example, Val1691Arg results in a 32-fold reduction in ISG15-AMC hydrolysis and nearly a 2000-fold reduction in Ub-AMC hydrolysis. Bailey-Elkin et al. previously showed that Val1691Arg completely abolishes the ability of PLpro to antagonize IFN, as it no longer suppressed the IFN-β promoter in cells and mimicked the catalytically dead enzyme (Bailey-Elkin et al., 2014). The loss of IFN antagonism was attributed to loss of DUB activity but deISG activity was not determined.

Based on our results, the loss of IFN antagonism could be due to either the loss of either DUB or deISG activity or both. In general, inserting a negatively or positively charged residue into the hydrophobic pocket of ISG15 is found not to be favored. In the case of binding Ub, only a positive charge is not permitted, as this would introduce charge-charge repulsion with Arg42 of Ub. To delineate if the observed effects of an insertion of an arginine at position 1691 was simply due to a bulk or steric overlap effect, Val1691 was also mutated to a phenylalanine. Surprisingly, Val1691Phe showed a 13-fold increase in the k_{cat} value for Ub-AMC while other activities were similar to the wild-type. Structurally, Phe1691 would allow for an additional π-cation interaction with Arg42 of Ub. On the other hand, engineering a more conservative mutation i.e. a small polar serine at the Val1691 position only reduced the ISG15-AMC efficiency (6.2-fold based on the k_{app} value) while Ub-AMC efficiency was less affected. TheVal1691Ser mutant did not reach saturation for either Ub-AMC or ISG15-AMC; the loss in efficiency was primarily due to an increase in K_m for ISG15 (Fig. 4B and Table 2). The selectivity of Val1691Ser mutant towards ISG15-AMC decreased by 3.8-fold compared to the wild-type and is the only mutant that has similar catalysis for both substrates. This more conservative mutation also restored RLRGG-AMC activity back to that of the wild-type. We suggest that position 1691 in PLpro is critical for substrate recognition, and based on the amino acid substitution at position 1691, it is possible to selectively modulate PLpro deISG (Val1691Asp, Val1691Ser) or DUB (Val1691Phe) activities or disrupt both DUB/deISG activities simultaneously (Val1691Arg, Val1691Lys).

His1652Ala, which is structurally adjacent to that of Val1691, did not significantly alter the enzymatic profile of MERS-CoV PLpro in our initial screening (Fig. 4A). We originally thought that the hydrophobic contacts and water-mediated interactions made by His1652 were not significant, but instead of performing alanine scanning, we sought to disrupt MERS-CoV PLpro activity by inserting a charged and bulky residue at this position as done with Val1691. Excitingly, mutation of the His1652 to an arginine drastically impaired both PLpro DUB/deISG activities by ~300-400-fold, a similar trend to the Val1691Arg and Val1691Lys mutants. In fact, to observe hydrolysis of these substrates, a higher concentration of enzyme was required and nearly approached the concentration of substrate in the assay. His1652Arg also exhibited a 4-fold reduction in RLRGG-AMC activity. In general, placing a bulky and charged residue in this region of PLpro does affect the active site functionality to a certain degree. We also analyzed if the water-mediated contacts involving His1652 were important by mutating this residue to a phenylalanine, which is incapable of hydrogen bonding. His1652Phe showed only a 1.7-fold decrease in catalytic efficiency for both ISG15-AMC and Ub-AMC. Interestingly, His1652Phe had a lower K_m value than wild-type for Ub-AMC (1.8 μM versus 16.6 μM) suggesting a 9-fold increase in binding affinity for this substrate, but there was also a 5.5-fold decrease in k_{cat} (Fig. 4D and Table 2). Overall, the net change was an increase in the catalytic efficiency for Ub-AMC about 2-fold over that for the wild-type enzyme. We observed a similar trend for Val1691Phe catalysis towards ISG15-AMC, but it was not as pronounced (Fig. 4B and Table 2). Overall, PLpro catalytic activity is more sensitive to having a positively charged amino acid at position 1652 rather than a smaller or bulky hydrophobic residue.

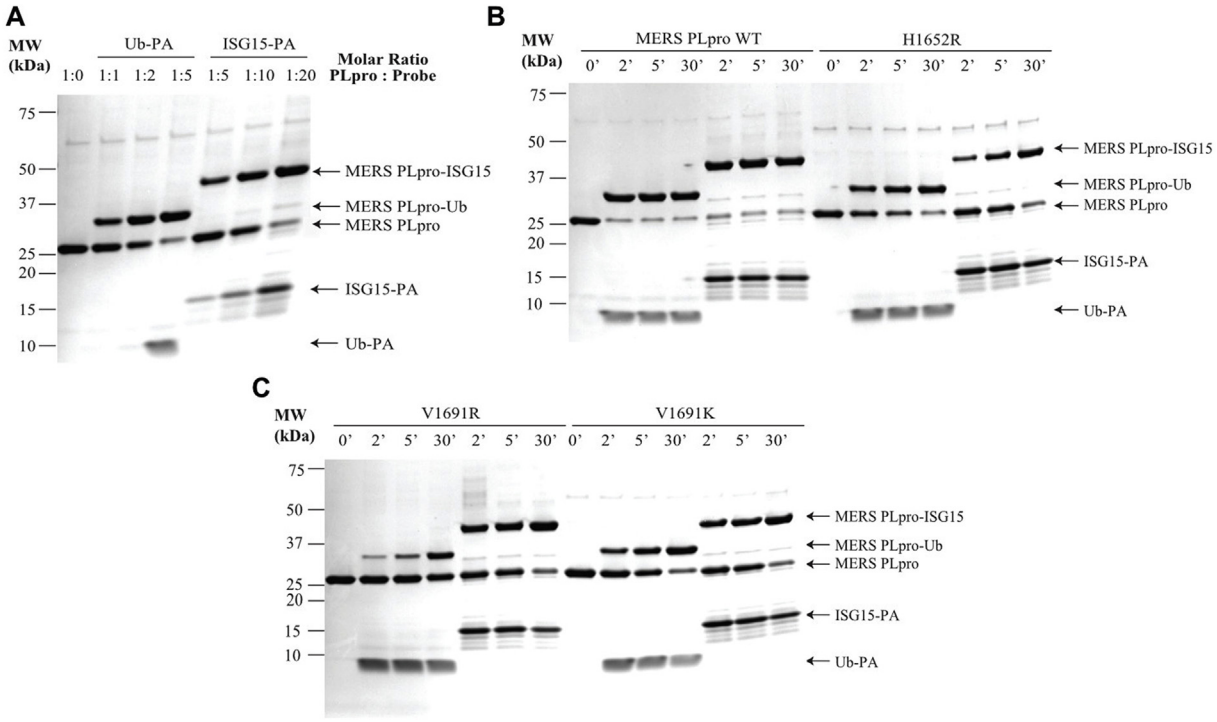

Fig. 5. Defects in Ub-PA and ISG15-PA probe reactivity by DUB/deISG deficient mutants. (A) Coomassie-blue stained SDS-PAGE gel of the MERS PLpro wild-type reactivity towards Ub-PA and ISG15-PA at different molar ratios of PLpro to probe after a 1 h incubation. Ratio 1:0 serves as the negative control, which only contains 5 μM PLpro. (B–C) Reactivity of MERS PLpro wild-type and mutants toward Ub-PA (ratio 1:5) and ISG15-PA (ratio 1:20) at different time points (2, 5, and 30 min) from three independent experiments visualized by Coomassie-Blue stained SDS-PAGE gel. PLpro without addition of the PA probe served as the negative control (0′).

To further evaluate the DUB/deISG deficiencies of the His1652Arg, Val1691Arg, and Val1691Lys mutants, their ability to react and form a covalent modification with Ub-PA and ISG15-PA were tested. First, the optimal molar ratio required for complete conversion to the covalent adduct was determined using the MERS PLpro wild-type. Within a 1 h incubation reaction, MERS PLpro-wild-type was completely modified by Ub-PA and ISG15-PA at a 1:5 ratio and 1:20 ratio, respectively (Fig. 5A). These molar ratios were then used to analyze the reactivity of the mutants at different time points. While wild-type MERS PLpro was capable of being converted fully to complexes with both Ub-PA and ISG15-PA within a short 2 min incubation, all three mutants showed impaired reactivity at the earlier time points (Fig. 5B and C). All mutants still showed unreacted PLpro at the 5 min incubation with ISG15-PA. For the His1652Arg and Val1691Lys mutants, impaired reactivity at 5 min was also observed with Ub-PA, as a portion of complex was converted (Fig. 5B and C). For Val1691Arg, even after a 30 min prolonged incubation, unreacted PLpro was still visible on the gel while the dominant band was complex with the other mutants and wild-type (Fig. 5B and C). This single mutation elicited a similar defect in the reaction with Ub-PA as that of $USP18^{IBB-1-USP7}$ with ISG15-PA, which contained four mutations in the ISG15-binding box 1 (IBB-1) (Basters et al., 2017). From these data, all three mutants are impaired for Ub/ISG15-PA reactivity. Consistent with our kinetic data, the Val1691Arg mutation may target DUB activity more so than deISG activity, and it shows a striking defect in Ub-PA reactivity.

With the goal of creating a PLpro mutant that lacks DUB activity but retains deISG activity, we focused on residue Thr1653 as we observed from the X-ray structure that this residue only engages with the Ub substrate and not ISG15. The Thr1653Arg mutant was partially characterized previously and was shown to be deficient in DUB activity but it was not tested for deISG activity (Bailey-Elkin et al., 2014). In addition, Thr1653Arg significantly inhibits PLpro-mediated IFN-antagonism in cells, but not quite to the extent of a Val1691Arg mutant (Bailey-Elkin et al., 2014). From the kinetic studies presented in Fig. 4D, the Thr1653Arg mutant cannot be saturated with the Ub-AMC substrate over the concentration ranges tested. Thr1653Arg exhibits a 4.1-fold reduction in Ub-AMC catalytic efficiency compared to the wild-type and only a small reduction in ISG15-AMC activity (Table 2). These results suggest that the observed decrease in DUB activity in cells for Thr1653Arg is likely what caused the suppression of IFN-β promoter rather than a loss in deISG activity.

To delineate if the reduction in DUB catalytic activity was due to substituting a bulkier residue rather than a charged residue, we mutated Thr1653 to a phenylalanine. The kinetic data in Table 2 show that there are no significant effects on catalysis supporting the idea that it is the insertion of a positively charged residue at this position that is detrimental to DUB activity. Insertion of arginine at 1653 places it in close proximity to Arg42 of Ub and to a guanidinium stacking interaction between Arg1649 of PLpro and Arg72 of Ub. The net effect is a charge repulsion that decreases substrate binding and catalysis.

To probe the importance of Arg1649 of PLpro and its involvement in DUB and deISG activities, this residue was mutated to an alanine. Arg1649Ala exhibited a 18.5-fold and 3.9-fold enhancement in Ub-AMC and peptide efficiencies while its ISG15-AMC efficiency was not affected (Table 2). This is a surprising observation due to the fact that arginine likely interacts with the P5 arginine in the RLRGG motif of all three substrates. It is possible that removing the stacked guanidinium group interaction alleviates any electrostatic repulsion with Arg42 in Ub so that Ub is more easily accommodated. Conversely, since there is no extra charge at the equivalent Arg42 position in ISG15, the charged guanidinium groups are more properly balanced by negatively charged residues, such as Asp1645 and interacting waters. Therefore, the local environment of Arg1649 appears to differ when binding to each of these substrates.

Since SARS-CoV PLpro has a glutamate at the equivalent Arg1649 position, we thought that engineering MERS to be more SARS-like would also enhance its activity. Indeed, Arg1649Glu exhibited a similar trend as Arg1649Ala, 17-fold and 8.4-fold enhancement in Ub-AMC and

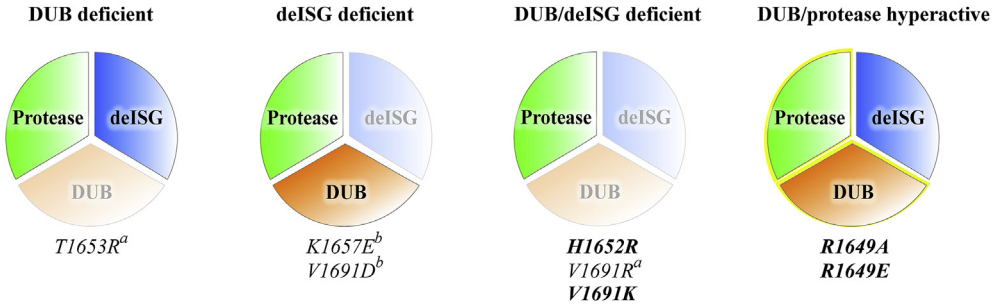

Fig. 6. Functional tools of different MERS-CoV PLpro mutants investigated to date that are characterized as selectively DUB or deISG deficient, both DUB and deISG deficient, or are both DUB and protease hyperactive mutations. A pie-chart is used to represent the multifunctional activities of PLpro. New sites of mutation investigated in this study are bolded. [a]PLpro mutants first investigated by Bailey-Elkin, B.A. et al. 2014. [b]Mutants previously characterized from Daczkowski, C.M. et al. 2017b.

peptide activity, while its ISG15-AMC activity was less effected. Both Arg1649Ala and Arg1649Glu exhibited nearly a 15-fold enhancement in K_m for Ub (Table 2 and Fig. 4C). These newly identified hyperactive DUB mutants have altered selectivity compared to the wild-type and favor Ub rather than ISG15 by 4 to 5-fold. In fact, these mutants have over 5-fold higher efficiency of hydrolysis towards Ub-AMC compared to SARS-CoV PLpro wild-type and similar efficiency to a hyperactive DUB mutant Arg167Glu previously characterized in SARS-CoV PLpro, which would also introduced an additional counter ion in this region near Arg42 of Ub (Daczkowski et al., 2017a). These results provide insight into how to change MERS-CoV PLpro selectivity from ISG15 to Ub without affecting its deISG activity.

Altogether, from our data and previous studies, MERS-CoV PLpro mutants that are selectively DUB deficient, selectively deISG deficient, and both DUB/deISG deficient have been identified that fit each category (Fig. 6). These mutants can now be used as functional tools to probe for the individual contributions of DUB and deISG activity to MERS-CoV replication and pathogenesis. It would be interesting to investigate whether partial or complete knockdown of both DUB/deISG activities or abolishing only one activity of PLpro is necessary to efficiently inhibit host cell antagonism and attenuate the MERS virus. Since there are additional IFN antagonists in the CoV genome, additional mutations targeting other viral proteins may be required.

A more provocative question would be whether PLpro mutants with enhanced DUB and protease activity could potentially enhance or exacerbate virus pathogenesis. Since these mutations do not exist in nature, it is possible that a DUB hyperactive virus may be nonviable or cannot be recovered using a reverse genetics system. Alternatively, this virus may reach a steady-state through reversion or mutation to survive and continue to replicate in the host population. More studies that evaluate these PLpro mutants in animal models are needed to answer these important biological questions and to explore the potential for using such mutants for the design and development of live-attenuated vaccines.

4. Conclusions

The X-ray crystal structure of MERS-CoV PLpro-ISG15 and the design of PLpro mutants with attenuated DUB and/or deISG activities provide critical structural and functional data and new functional tools for delineating the importance of DUB versus deISG activity in MERS-CoV pathogenesis and replication. MERS-CoV PLpro only actively engages with the C-terminal domain of ISG15 utilizing one SUb1 subsite, in contrast to SARS-CoV PLpro that appears to engage with the N-terminus of ISG15 using a second SUb2 subsite. MERS-CoV PLpro recognizes a hydrophobic surface on ISG15 that is distinct from the hydrophobic patch on Ub. Insertion of a charged residue into PLpro that contacts the hydrophobic region in ISG15 decreases specificity. Selectively disrupting or enhancing the DUB activity of PLpro can be accomplished by inserting a positive charge at position 1653 or removing the charge of Arg1649, respectively. Thr1653Arg will be a useful mutation for probing the role of DUB activity in MERS pathogenesis. Mutation of either His1652 or Val1691 to a positive charged residue completely impairs both DUB and deISG activities making either mutant useful for probing the contribution of both activities. DUB/deISG deficient mutants, His1652Arg, Val1691Lys, and Val1691Arg characterized in this study will be good candidates for investigating the potential for attenuating the MERS virus and may be useful for live-attenuated vaccine design.

Acknowledgements

Research reported in this publication was supported by the National Institute of Allergy and Infectious Disease of the National Institutes of Health under award number R01AI085089. ADM also wishes to also acknowledge partial support from the Center for Structural Genomics of Infectious Disease (NIH-NIAID Contract HHSN272201700060C and the Walther Cancer Foundation. Crystallization and DNA sequencing were partially supported by the Purdue Center for Cancer Research Macromolecular Crystallography and DNA Sequencing Shared Resources which are partially supported by NIH grant P30 CA023168.X-ray data were collected at the Life Sciences Collaborative Access Team beamline 21-ID-D at the Advanced Photon Source, Argonne National Laboratory. The Advanced Photon Source, a U.S. Department of Energy (DOE) Office of Science User Facility operated for the DOE Office of Science by Argonne National Laboratory under Contract No. DE-AC02-06CH11357. Use of the LS-CAT Sector 21 was supported by the Michigan Economic Development Corporation and the Michigan Technology Tri-Corridor (Grant 085P1000817).

Appendix A. Supplementary data

Supplementary data to this article can be found online at https://doi.org/10.1016/j.antiviral.2019.104661.

References

Afonine, P.V., Grosse-Kunstleve, R.W., Echols, N., Headd, J.J., Moriarty, N.W., Mustyakimov, M., Terwilliger, T.C., Urzhumtsev, A., Zwart, P.H., Adams, P.D., 2012. Towards automated crystallographic structure refinement with phenix.refine. Acta Crystallogr D Biol Crystallogr 68, 352–367.

Akutsu, M., Ye, Y., Virdee, S., Chin, J.W., Komander, D., 2011. Molecular basis for ubiquitin and ISG15 cross-reactivity in viral ovarian tumor domains. Proc. Natl. Acad. Sci. U. S. A. 108, 2228–2233.

Bailey-Elkin, B.A., Knaap, R.C., Johnson, G.G., Dalebout, T.J., Ninaber, D.K., van Kasteren, P.B., Bredenbeek, P.J., Snijder, E.J., Kikkert, M., Mark, B.L., 2014. Crystal structure of the Middle East respiratory syndrome coronavirus (MERS-CoV) papain-like protease bound to ubiquitin facilitates targeted disruption of deubiquitinating activity to demonstrate its role in innate immune suppression. J. Biol. Chem. 289, 34667–34682.

Basters, A., Geurink, P.P., Röcker, A., Witting, K.F., Tadayon, R., Hess, S., Semrau, M.S., Storici, P., Ovaa, H., Knobeloch, K.P., Fritz, G., 2017. Structural basis of the specificity of USP18 toward ISG15. Nat. Struct. Mol. Biol. 24, 270–278.

Báez-Santos, Y.M., Mielech, A.M., Deng, X., Baker, S., Mesecar, A.D., 2014. Catalytic function and substrate specificity of the papain-like protease domain of nsp3 from the Middle East respiratory syndrome coronavirus. J. Virol. 88, 12511–12527.

Békés, M., van der Heden van Noort, G.J., Ekkebus, R., Ovaa, H., Huang, T.T., Lima, C.D., 2016. Recognition of Lys48-linked Di-ubiquitin and deubiquitinating activities of the SARS coronavirus papain-like protease. Mol. Cell 62, 572–585.

Chan, J.F., Lau, S.K., To, K.K., Cheng, V.C., Woo, P.C., Yuen, K.Y., 2015. Middle East respiratory syndrome coronavirus: another zoonotic betacoronavirus causing SARS-like disease. Clin. Microbiol. Rev. 28, 465–522.

Chen, L., Borozan, I., Feld, J., Sun, J., Tannis, L.L., Coltescu, C., Heathcote, J., Edwards, A.M., McGilvray, I.D., 2005. Hepatic gene expression discriminates responders and nonresponders in treatment of chronic hepatitis C viral infection. Gastroenterology 128, 1437–1444.

Clasman, J.R., Báez-Santos, Y.M., Mettelman, R.C., O'Brien, A., Baker, S.C., Mesecar, A.D., 2017. X-ray structure and enzymatic activity profile of a core papain-like protease of MERS coronavirus with utility for structure-based drug design. Sci. Rep. 7, 40292.

Clementz, M.A., Chen, Z., Banach, B.S., Wang, Y., Sun, L., Ratia, K., Baez-Santos, Y.M., Wang, J., Takayama, J., Ghosh, A.K., Li, K., Mesecar, A.D., Baker, S.C., 2010. Deubiquitinating and interferon antagonism activities of coronavirus papain-like proteases. J. Virol. 84, 4619–4629.

Daczkowski, C.M., Dzimianski, J.V., Clasman, J.R., Goodwin, O., Mesecar, A.D., Pegan, S.D., 2017a. Structural insights into the interaction of coronavirus papain-like proteases and interferon-stimulated gene product 15 from different species. J. Mol. Biol. 429, 1661–1683.

Daczkowski, C.M., Goodwin, O., Dzimianski, J.V., Farhat, J.J., Pegan, S.D., 2017b. Structurally guided removal of deISGylase biochemical activity from papain-Like protease originating from the Middle East Respiratory Syndrome Virus. J. Virol. 91 e01067-01017.

Durfee, L.A., Lyon, N., Seo, K., Huibregtse, J.M., 2010. The ISG15 conjugation system broadly targets newly synthesized proteins: implications for the antiviral function of ISG15. Mol. Cell 38, 722–732.

Emsley, P., Cowtan, K., 2004. Coot: model-building tools for molecular graphics. Acta Crystallogr D Biol Crystallogr 60, 2126–2132.

Fehr, A.R., Channappanavar, R., Perlman, S., 2017. Middle East respiratory syndrome: emergence of a pathogenic human coronavirus. Annu. Rev. Med. 68, 387–399.

Giannakopoulos, N.V., Arutyunova, E., Lai, C., Lenschow, D.J., Haas, A.L., Virgin, H.W., 2009. ISG15 Arg151 and the ISG15-conjugating enzyme UbE1L are important for innate immune control of Sindbis virus. J. Virol. 83, 1602–1610.

Hermann, M., Bogunovic, D., 2017. ISG15: in sickness and in Health. Trends Immunol. 38, 79–93.

Komander, D., Rape, M., 2012. The ubiquitin code. Annu. Rev. Biochem. 81, 203–229.

Lai, C., Struckhoff, J.J., Schneider, J., Martinez-Sobrido, L., Wolff, T., García-Sastre, A., Zhang, D.E., Lenschow, D.J., 2009. Mice lacking the ISG15 E1 enzyme UbE1L demonstrate increased susceptibility to both mouse-adapted and non-mouse-adapted influenza B virus infection. J. Virol. 83, 1147–1151.

Lei, J., Mesters, J.R., Drosten, C., Anemüller, S., Ma, Q., Hilgenfeld, R., 2014. Crystal structure of the papain-like protease of MERS coronavirus reveals unusual, potentially druggable active-site features. Antivir. Res. 109, 72–82.

McCoy, A.J., Grosse-Kunstleve, R.W., Adams, P.D., Winn, M.D., Storoni, L.C., Read, R.J., 2007. Phaser crystallographic software. J. Appl. Crystallogr. 40, 658–674.

Mielech, A.M., Kilianski, A., Baez-Santos, Y.M., Mesecar, A.D., Baker, S.C., 2014. MERS-CoV papain-like protease has deISGylating and deubiquitinating activities. Virology 450–451, 64–70.

Minor, W., Cymborowski, M., Otwinowski, Z., Chruszcz, M., 2006. HKL-3000: the integration of data reduction and structure solution–from diffraction images to an initial model in minutes. Acta Crystallogr D Biol Crystallogr 62, 859–866.

Narasimhan, J., Wang, M., Fu, Z., Klein, J.M., Haas, A.L., Kim, J.J., 2005. Crystal structure of the interferon-induced ubiquitin-like protein ISG15. J. Biol. Chem. 280, 27356–27365.

Perng, Y.C., Lenschow, D.J., 2018. ISG15 in antiviral immunity and beyond. Nat. Rev. Microbiol. 16, 423–439.

Ratia, K., Kilianski, A., Baez-Santos, Y.M., Baker, S.C., Mesecar, A., 2014. Structural Basis for the Ubiquitin-Linkage Specificity and deISGylating activity of SARS-CoV papain-like protease. PLoS Pathog. 10, e1004113.

Speer, S.D., Li, Z., Buta, S., Payelle-Brogard, B., Qian, L., Vigant, F., Rubino, E., Gardner, T.J., Wedeking, T., Hermann, M., Duehr, J., Sanal, O., Tezcan, I., Mansouri, N., Tabarsi, P., Mansouri, D., Francois-Newton, V., Daussy, C.F., Rodriguez, M.R., Lenschow, D.J., Freiberg, A.N., Tortorella, D., Piehler, J., Lee, B., García-Sastre, A., Pellegrini, S., Bogunovic, D., 2016. ISG15 deficiency and increased viral resistance in humans but not mice. Nat. Commun. 7, 11496.

Studier, F.W., 2005. Protein production by auto-induction in high density shaking cultures. Protein Expr. Purif. 41, 207–234.

van Kasteren, P.B., Bailey-Elkin, B.A., James, T.W., Ninaber, D.K., Beugeling, C., Khajehpour, M., Snijder, E.J., Mark, B.L., Kikkert, M., 2013. Deubiquitinase function of arterivirus papain-like protease 2 suppresses the innate immune response in infected host cells. Proc. Natl. Acad. Sci. U. S. A. 110 E838-847.

WHO, 2018. Middle East Respiratory Syndrome (MERS-CoV).

Wilkinson, K.D., Gan-Erdene, T., Kolli, N., 2005. Derivitization of the C-terminus of ubiquitin and ubiquitin-like proteins using intein chemistry: methods and uses. Methods Enzymol. 399, 37–51.

Zhang, X., Bogunovic, D., Payelle-Brogard, B., Francois-Newton, V., Speer, S.D., Yuan, C., Volpi, S., Li, Z., Sanal, O., Mansouri, D., Tezcan, I., Rice, G.I., Chen, C., Mansouri, N., Mahdaviani, S.A., Itan, Y., Boisson, B., Okada, S., Zeng, L., Wang, X., Jiang, H., Liu, W., Han, T., Liu, D., Ma, T., Wang, B., Liu, M., Liu, J.Y., Wang, Q.K., Yalnizoglu, D., Radoshevich, L., Uzé, G., Gros, P., Rozenberg, F., Zhang, S.Y., Jouanguy, E., Bustamante, J., García-Sastre, A., Abel, L., Lebon, P., Notarangelo, L.D., Crow, Y.J., Boisson-Dupuis, S., Casanova, J.L., Pellegrini, S., 2015. Human intracellular ISG15 prevents interferon-α/β over-amplification and auto-inflammation. Nature 517, 89–93.

Zhao, C., Collins, M.N., Hsiang, T.Y., Krug, R.M., 2013. Interferon-induced ISG15 pathway: an ongoing virus-host battle. Trends Microbiol. 21, 181–186.

Zheng, L., Baumann, U., Reymond, J.L., 2004. An efficient one-step site-directed and site-saturation mutagenesis protocol. Nucleic Acids Res. 32, e115.